Journal of
Materials Chemistry A

ROYAL SOCIETY
OF CHEMISTRY

PAPER

View Article Online
View Journal | View Issue

Cite this: *J. Mater. Chem. A*, 2023, **11**, 10346

Rapid synthesis of efficient Mo-based electrocatalyst for the hydrogen evolution reaction in alkaline seawater with 11.28% solar-to-hydrogen efficiency†

Zhan Zhao,[a] Jianpeng Sun,[a] Zizhen Li,[a] Xiaofeng Xu,[c] Zisheng Zhang,[b] Chunhu Li,[a] Liang Wang[a] and Xiangchao Meng*[a]

Received 13th March 2023
Accepted 18th April 2023

DOI: 10.1039/d3ta01522j

rsc.li/materials-a

Herein, we applied a rapid Joule heating method to fabricate $MoNi_4$ nanoparticles anchored on MoO_x nanorods ($MoNi_4/MoO_x$) for the electrocatalytic splitting of seawater. Compared to the traditional calcination method, the Joule heating method not only shortened the preparation time, but also modulated the chemical states of the reactive sites and further improved the electrocatalytic activity. As-prepared $MoNi_4/MoO_x$ achieved overpotentials of 15 mV (@10 mA cm^{-2}) and 227 mV (@1000 mA cm^{-2}) in alkaline seawater electrolyte for the hydrogen evolution reaction. This composite also exhibited excellent chemical stability in 1000 h testing at a constant current density of 1 A cm^{-2}. Moreover, the $MoNi_4/MoO_x$ showed great performance in a membrane electrode assembly (MEA) electrochemical reactor, which reduced the energy needed by 3.33 kW h to generate per cubic meter of H_2 at a current density of 200 mA cm^{-2} relative to a commercial Ni foam system. Finally, a home-made solar power-assisted water splitting device was successfully constructed using $MoNi_4/MoO_x//RuO_2$ electrodes and polymer solar cells (PSCs), achieving a solar-to-hydrogen (STH) efficiency of 11.28%.

Introduction

The ever-rising environmental pollution and energy-shortage crisis are attracting scientists' attention to the research into attractive renewable hydrogen energy (H_2), due to its high energy density (~130 MJ kg^{-1}).[1–3] Currently, the production of H_2 by electrochemical seawater splitting has emerged as one of the most promising strategies.[4–7] Over the past decade, commercial Pt/C has been regarded as the state-of-the-art hydrogen evolution reaction (HER) electrocatalyst in alkaline water splitting. Unfortunately, its high cost and barely satisfactory elemental abundance hampers its large-scale implementation. To date, great efforts have been devoted to the exploration of non-precious metal-based electrocatalyst, which can be reasonably constructed using transition metals, such as the earth-abundant W, Fe, Co, Ni, and Mo, and these have consequently been at the forefront of research.[8,9] However, their sluggish kinetics and high energetic barrier dramatically impede the HER activity of such electrocatalysts in seawater splitting. Meanwhile, due to the catalyst deactivation caused by the complexity of dissolved cations and insoluble precipitates, it is still a challenge to construct highly active and stable electrocatalysts for seawater splitting. Therefore, it remains imperative to devote more effort to exploring cost-effective, highly efficient, and robust electrocatalysts to expedite the seawater splitting process, so as to realize the large-scale production of H_2.[10]

Notably, Mo-based compounds, including sulfides,[11] phosphides,[12] selenides,[9] oxides,[13] and carbides,[14] have been investigated as promising candidates in the field of seawater electrolysis, which benefited from having an option for Pt-like d-bands electrical assembly, numerous accessible active sites, and excellent stability in harsh environments.[15] Among these electrocatalysts, molybdenum oxide has attracted great attention due to its advantages of faster charge-carrier transportation and abundant active sits provided by Mo-edge and O-edge, albeit its inappropriate adsorption energy for hydrogen hamper its use as a competitive electrocatalyst.[16] As reported, the adsorption energy of hydrogen could be optimized *via* a "d electron complementary effect", wherein the combination of Mo species with Ni can play an important role in modulating the surface charge states, leading to ideal binding free energies with reactive intermediates.[17–19] For instance, Feng and co-workers

---

[a] *Key Laboratory of Marine Chemistry Theory and Technology (Ministry of Education), College of Chemistry & Chemical Engineering, Ocean University of China, Qingdao, 266100, China. E-mail: mengxiangchao@ouc.edu.cn*

[b] *Department of Chemical and Biological Engineering, Faculty of Engineering, University of Ottawa, Ottawa, Ontario, K1N6N5, Canada*

[c] *College of Materials Science and Engineering, Ocean University of China, Qingdao, 266100, China*

† Electronic supplementary information (ESI) available. See DOI: https://doi.org/10.1039/d3ta01522j

attempted to fabricate a $MoNi_4$ alloy anchored on MoO_2 cuboids *via* a calcination method at 500 °C for 2 h, which required an overpotential of 15 mV to drive a current density of 10 mA cm^{-2} for the HER.[20] Wang *et al.* fabricated a MoNi alloy supported on hollow MoO_2 nanorods by a two-step annealing for over 5 h, wherein the reduced energy barrier through a synergistic action of Mo and Ni was obtained, leading to a low energy equivalent input.[21] Given these series of great advancements, Mo, Ni-based catalysts for seawater electrolysis have been recently reported. Electrocatalysts are usually obtained by traditional temperature-programmed calcination methods in electric furnaces,[22] which are typically limited by a slow heating/cooling rate, high energy consumption, and cumbersome production process.[23] Typically, the sequential reduction might occur during the slow heating process, due to the different reduction potential between the Ni and Mo species, thus leading to a uniform distribution of active sites.[24] For instance, Hu *et al.* found that the Ni element was distributed in a granular pattern on the surface of the nanorods in the process of synthesizing $MoNi_4/MoO_{3-x}$ nanorods.[25] Besides, the active sites and mechanical stability of the as-synthesized catalysts might be inevitably deteriorated by the agglomeration, surface oxidation, and weak interactions with the substrate, which could not allow them to adapt to the high current densities (200 to 1000 mA cm^{-2}), ultralong operation duration (>600 h) and elevated temperature (>50 °C) needed for commercial advanced alkaline water electrolyzers.[26] Thus, synthesizing highly active catalysts with the prospect of industrial application by low-cost, effective methodologies is still recognized as a challenge.

Recently, the Joule heating method has been considered as an innovative and highly efficient method based on electrical Joule heating. The target temperature could be provided in an ultrashort treatment time, which might overcome the uneven distribution of active sites due to the difference in reduction potential.[27] Besides, the high-temperature-variation rate can not only avoided the agglomeration and unstable dispersion, but also endow the resultant catalyst with structural advantages, such as oxygen vacancies and stacking faults, which would be potentially beneficial to the HER performance. Chen *et al.* proposed a facile high-temperature-assisted strategy to convert iron pyrite into uniformly distributed nanostructured FeS_2, which exhibited highly superior electrochemistry (139 mV @ 10 mA cm^{-2}).[28] Fei *et al.* prepared a Co–N–C single-atom monolith *via* ultrafast Joule heating, wherein the instantaneous quenching played an important role in achieving a stable atomic-scale dispersion so as to avoid the blockage of active sites.[29]

In this work, we employed a rapid Joule heating approach to achieve a freestanding electrocatalyst ($MoNi_4/MoO_x$) grown on Ni foam for seawater electrolysis, wherein the $MoNi_4$ alloy nanoparticles could be anchored on MoO_x in an Ar–H_2 (10%) atmosphere. Proved by a series of electrochemical measurements, the $MoNi_4/MoO_x$ exhibited outstanding electrocatalytic performance under alkaline seawater conditions. In particular, the as-prepared $MoNi_4/MoO_x$ was characterized with an ultralow overpotential of 15 mV (227 mV) for generating a current density of 10 mA cm^{-2} (1 A cm^{-2}), which was superior to $MoNi_4/MoO_x$-T synthesized by the traditional temperature-programmed calcination method. Combined with first-principles calculations, it was found that a high content of Mo^{4+} was preferred to optimize the adsorption state, leading to an improved intrinsic activity of $MoNi_4/MoO_x$. Besides, to highlight the feasibility for industrial application, the $MoNi_4/MoO_x$ allow was applied as a cathode in a commercial membrane electrode assembly (MEA) stack, which could save 3.33 kW h m^{-3} energy at a current density of 200 mA cm^{-2} compared with the commercial Ni foam. Finally, combining our $MoNi_4/MoO_x$ electrode with a tandem home-made PSC, we successfully fabricated a solar power-assisted water splitting device with a high STH of 11.28%, which is promising to compete in the global carbon neutral economy. This research exhibits a breakthrough in the synthesis of active commercial electrocatalysts by a low-cost method for industrial application.

Results and discussion

Fig. 1a displays the Joule heating setup, wherein the different precursors were placed in a molybdenum boat, and the conductive graphite block was used as the electrode. The reaction chamber was pumped into a vacuum before the reducing gas was injected. During the process, rapid electrical Joule heating was generated leading to the target reaction temperature with a high heating/cooling rate. To highlight the difference between the Joule heating and traditional calcination, the heating rate was plotted, as shown in Fig. 1b and S1.† Compared with the traditional heating process, the target reaction temperature could be instantaneously obtained at a ramp rate of 67 °C s^{-1} from room temperature, which was promoted by the Joule heating. On the other hand, such a short treatment time not only led to an efficient synthesis process, but also meant a lower energy consumption, which only consumed 0.12% energy of the traditional method (Fig. 1b).

Structural characterization of $MoNi_4/MoO_x$

The processes of preparing $MoNi_4/MoO_x$ is schematically illustrated in Fig. 2a. The cleaned Ni foam (donated as NF) was selected as a three-dimensional support for the coordination of ammonium molybdate and nickel nitrate, which was obtained through a hydrothermal reaction. As characterized by scanning electron microscopy (SEM) in Fig. 2b, it could be seen that the $NiMoO_4$ precursor was a dense nanorods-like structure with a smooth surface vertically aligned on the NF matrix, which collectively formed nanospheres with a diameter of 50–80 μm. The elements Ni, Mo, and O were uniformly distributed in the hybrids (Fig. S2†), wherein the atomic ratio of Ni : Mo : O ≈ 1 : 1.2 : 3, as confirmed by the X-ray spectroscopy (EDX) results (Fig. S3†). Fig. S4a† shows the X-ray diffraction (XRD) pattern of the precursor (PDF# 13-0128), indicating the successful synthesis of $NiMoO_4$.[30] Subsequent Joule heating under the reduction atmosphere rapidly dehydrated and decomposed the $NiMoO_4$ to $MoNi_4$ alloy and MoO_x (denoted as $MoNi_4/MoO_x$), which could be confirmed by the XRD pattern (PDF# 65-5480; PDF# 32-0671) in Fig. S4b.†[20] Due to the strong diffraction peaks attributed to the Ni foam (PDF# 04-0850),[31] the diffraction peaks

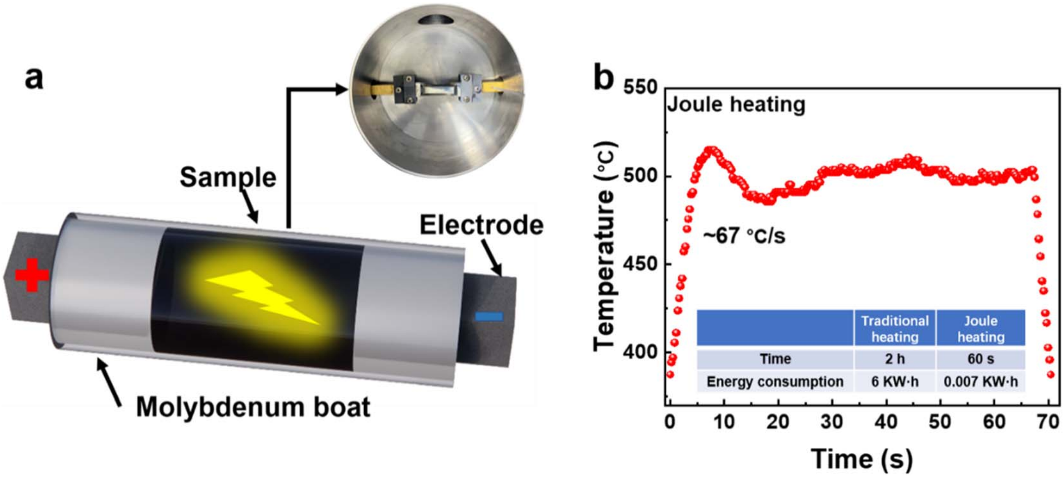

Fig. 1 (a) Schematic diagram of the Joule heating setup. (b) Real heating curves for the Joule heating method; the inset table exhibits the consumption of time and energy for the traditional heating and Joule heating methods (calculated by the equipment power multiplied by the heating time).

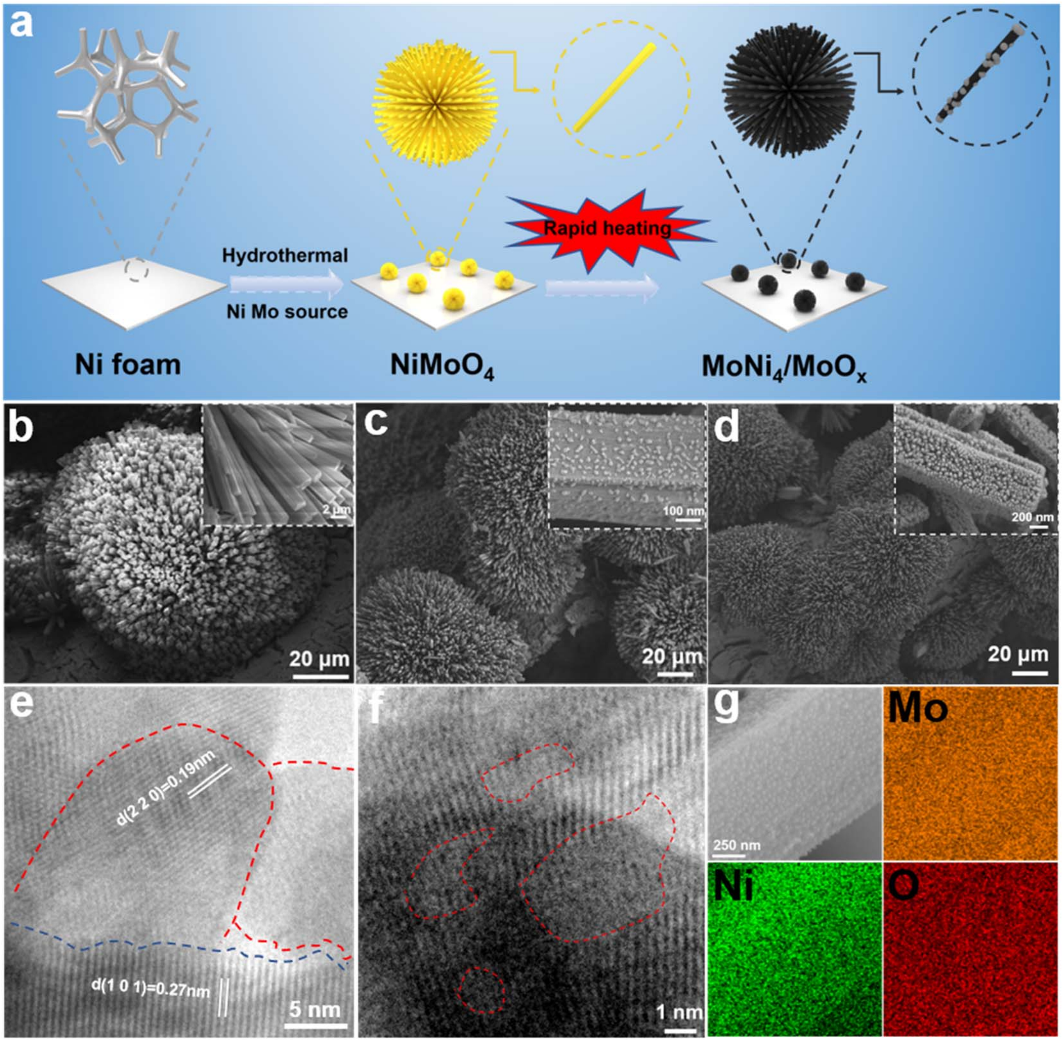

Fig. 2 (a) Schematic illustration of the synthesis process for $MoNi_4/MoO_x$; (b) SEM images of $NiMoO_4$; (c) SEM images of $MoNi_4/MoO_x$-T; (d) SEM images of $MoNi_4/MoO_x$; (e and f) TEM images of $MoNi_4/MoO_x$; (g) elemental mapping of $MoNi_4/MoO_x$.

of $MoNi_4$ were not obvious. Typically, it should be noted that the as-produced $MoNi_4/MoO_x$ well inherited the nanorods-like structure from the precursor as confirmed by the SEM image (Fig. 2d). In addition, the corresponding mapping (Fig. 2g) for the elements Ni, Mo, and O showed their uniform distribution on $MoNi_4/MoO_x$, wherein the atomic ratio of $Ni : Mo : O \approx 1 : 1 : 2$ as confirmed by the EDX result (Fig. S5†). It was worth noting that numerous $MoNi_4$ alloy particles in the range of $\sim$50 nm were attached to the surface nanorods, which increased the specific surface area, thus providing abundant active sites for the electrocatalytic reaction. More importantly, the porous and rough structure of $MoNi_4/MoO_x$ could be observed from Fig. 2d, indicating the increased accessible surface area and exposure of active sites, which could also be confirmed by the transmission electron microscopy (TEM) images (Fig. 2e and S6†). Clearly, from the TEM images, the lattice fringes with lattice distances (Fig. 2e and S7†) of 0.27 nm and 0.19 nm were assigned to the (1 0 1) plane of MoO_2 and the (2 2 0) plane of $MoNi_4$, respectively, which was consistent with the XRD results. Typically, numerous interconnected $MoNi_4$ nanoparticles (marked with red lines) were tightly anchored on the MoO_x, which not only formed the interface to facilitate the transfer of electrons as well as refining the intermediate binding capability, but also enhanced the mechanical stability during the electrocatalytic reaction.[32] Moreover, abundant defects could be clearly observed (Fig. 2f) which might have resulted from the rapid heating and cooling process.[31]

To emphasize the difference between the traditional heating and Joule heating, $MoNi_4/MoO_x$-T was synthesized by the traditional high-temperature calcination. Remarkably, XRD characterization showed that the $MoNi_4/MoO_x$-T had the same composition of $MoNi_4/MoO_x$ (Fig. S4c†). Also, the geometric morphologies of dense flower-like nanorods for $MoNi_4/MoO_x$-T were also revealed by SEM (Fig. 2c), wherein $MoNi_4$ nanoparticles with an average size of 51 nm were embedded on the substrate (Fig. S8a and b†). Despite the morphological similarity to $MoNi_4/MoO_x$-T, the $MoNi_4/MoO_x$ was characterized by smaller $MoNi_4$ nanoparticles with an average diameter of 46 nm and a porous surface (Fig. 2d, S8c and d†), in which the desirable morphology might be attributed to the rapid Joule heating. A small nanoparticle size usually indicates a large surface area and abundant active sites. Meanwhile, it has been proved that rational morphology engineering (such as fabricating a porous structure) is beneficial for the diffusion of the electrolyte as well as for achieving a specific surface area.[33,34] To verify the above conclusion, N_2 adsorption–desorption isotherm measurements were performed using the BET method, as shown in Fig. S9,† indicating that the specific surface area of the as-prepared $MoNi_4/MoO_x$ had a much larger value (16.9 m^2 g^{-1}) than for $MoNi_4/MoO_x$-T (9.1 m^2 g^{-1}), indicating the presence of rich surface-active sites, facilitated ion transport, and the likelihood of a rapid release of gases on the surface. The shape of the hysteresis loops indicated the presence of non-rigid aggregates of plate-like particles,[35] which provide sufficient active areas for the HER. The aperture distribution of $MoNi_4/MoO_x$ showed that the sizes of the mesopores mainly ranged from 4 to 20 nm (inset of Fig. S9†). In addition, the elements Ni, Mo, and O exhibited a poor dispersion on the surface of $MoNi_4/MoO_x$-T (Fig. S10†), while a uniform distribution and few agglomeration of $MoNi_4/MoO_x$ was obtained (Fig. 2g) due to the ultrafast heating/cooling rate treatment time in the Joule heating.[36] Such a differentiation might be caused by the reduction potentials of metal oxides.[24] During the reduction in a hydrogen atmosphere, the reductive reaction of Ni species preferentially occurred on the $NiMoO_4$ precursor due to the relevant lower standard molar enthalpies of formation (ΔH^Θ) than for Mo species, wherein the ΔH^Θ (298 K) of NiO was 240 kJ mol^{-1}, *i.e.*, much lower than the ΔH^Θ (298 K) of MoO_3 (1037 kJ mol^{-1}).[37] The target temperature obtained in such an ultrashort treatment time promoted the simultaneous reduction reaction of Mo and Ni, leading to a uniform distribution of active sites. The above results demonstrated that Joule heating treatment methods could achieve the formation of defects, and a uniform distribution of elements, as well as play an important role in morphology evolution for electrocatalysts.

X-Ray photoelectron spectroscopy (XPS) was performed next to further gain insights into the chemical state of $NiMoO_4$, $MoNi_4/MoO_x$, and $MoNi_4/MoO_x$-T. The presence of the Ni, Mo, and O elements in the as-prepared samples was verified by the XPS survey spectra in Fig. 3a and S11a,† which agreed with the EDS results. For the Mo 3d spectra, the $MoNi_4/MoO_x$ catalyst showed four valence states of Mo^{6+} (232.18 eV), Mo^{5+} (230.44 eV), Mo^{4+} (229.39 eV), and Mo^0 (228.04 eV) in Fig. 3b, revealing the reduction from the $NiMoO_4$ precursor (Fig. S11b†) *via* Joule heating in the reductive atmosphere.[38] Meanwhile, the relatively low valence states of Mo^{4+} and Mo^{5+} confirmed the presence of MoO_x accompanied with oxygen vacancies, which was favorable for the excitation of delocalized electrons to the conduction band, thus leading to enhanced conductivity.[39] Compared to $MoNi_4/MoO_x$-T ($Mo^{4+}/Mo^{5+} = 0.17 : 1$), the content of Mo^{4+} in $MoNi_4/MoO_x$ ($Mo^{4+}/Mo^{5+} = 0.90 : 1$) was much increased, meaning the concentration of surface Mo^{4+} was improved, leading to accelerated HER performance.[35] This might be due to the low empty d-orbital density of Mo^{4+} species in $MoNi_4/MoO_x$.[40] Such a superiority in electronic structure make it easier for H radicals to combine with Mo^{4+}, thus leading to enhanced HER performance, which was explored *via* subsequent DFT theoretical studies. Moreover, the peak moved to a higher binding energy, which meant that the heating method could regulate the electronic structure. For the Ni 2p spectra[41] (Fig. 3c), two groups of spin–orbit peaks were exhibited, which included Ni^{2+} ($2p_{3/2}$ and $2p_{1/2}$) peaks at 856.30 and 874.04 eV with satellite peaks at 862.13 and 880.38 eV, and others located at 852.86 and 870.22 eV, which were assigned to Ni^0. Compared to the $NiMoO_4$ (Fig. S11b and c†), the obvious signals of Ni^0 and Mo^0 suggested the formation of the $MoNi_4$ alloy after Joule heating in the reductive atmosphere.[25] For the O 1s spectra (Fig. 3d), obvious peaks at 530.51 and 531.68 eV were exhibited assigned to the lattice oxygen and oxygen vacancies, while another was observed located at 533.10 eV belonging to the H–O bond of the surface absorption species.[32] Notably, oxygen vacancies were generated in comparison with $NiMoO_4$ (Fig. S11d†), which might have been caused by the unsaturated coordination environment due to the presence of the low

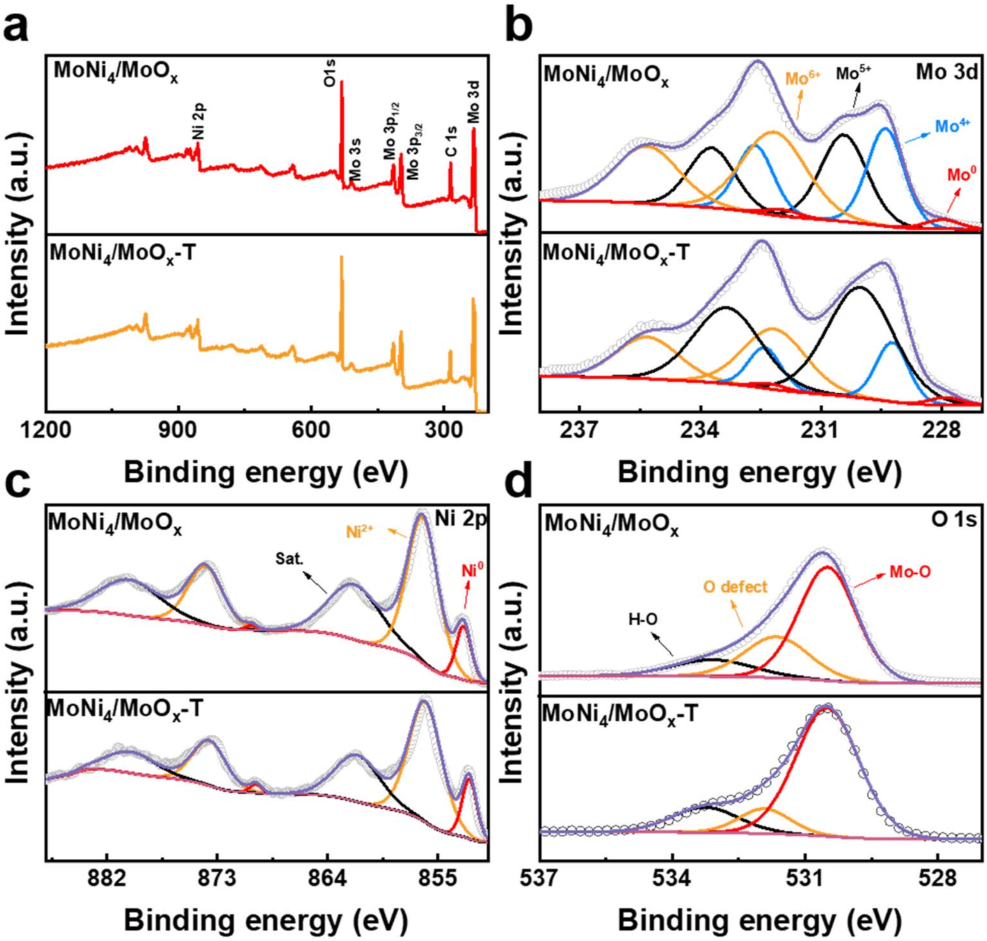

Fig. 3 XPS spectra of $MoNi_4/MoO_x$ and $MoNi_4/MoO_x$-T: (a) XPS survey spectra; (b) Mo 3d; (c) Ni 2p; and (d) O 1s.

valence states of Mo^{4+} and Mo^{5+}. Besides, the ratio of oxygen vacancies and lattice oxygen in $MoNi_4/MoO_x$ (0.4 : 1) was higher than in $MoNi_4/MoO_x$-T (0.15 : 1), indicating the presence of more abundant oxygen vacancies as shown in Fig. 3d, wherein the introduction of oxygen vacancies played an important role in tailoring the electronic structure to enhance the catalytic activity.

Investigation of the HER activities

In order to explore the electrocatalytic activities of $MoNi_4/MoO_x$ and $MoNi_4/MoO_x$-T, the HER performance was tested, wherein the electrocatalysts were applied as the working electrode in alkaline seawater electrolyte, respectively. Natural seawater was collected from the South Yellow Sea (35°55E, 120°42N), which contained 3.5% salts, and was further treated by KOH. The elemental composition and relative content are shown in Fig. S12a and b.† For comparison, Ni@NF, Mo@NF, and the benchmark Pt/C catalyst were also tested under the same conditions with $MoNi_4/MoO_x$. Fig. 4a shows the LSV curves. Encouragingly, the required overpotential for the current density of 10 mA cm^{-2} with $MoNi_4/MoO_x$ was only 15 mV in alkaline seawater electrolyte, exceeding that for Ni@NF, Mo@NF, Pt/C, and other reported catalysts[42–50] (Fig. 4b). We then verified the commerciality of $MoNi_4/MoO_x$ at a large current density of 1 A cm^{-2} in alkaline seawater, which only needed 227 mV, indicating a record activity in alkaline media (Fig. S13†).

Notably, $MoNi_4/MoO_x$ possessed a lower overpotential than $MoNi_4/MoO_x$-T (17 mV at 10 mA cm^{-2}), exhibiting that Joule heating was an advantageous and rapid approach for the synthesis of active electrocatalysts. Besides the porous morphology with a large specific surface area obtained *via* rapid Joule heating, the generated low-valence Mo^{4+} species played an important role too in effectively enhancing the efficiency for the HER. In order to exclude morphological effects, $MoNi_4/MoO_x$-30s and $MoNi_4/MoO_x$-90s with a low content of Mo^{4+} species were synthesized, which were regulated by different heating times. As shown in Fig. S14a,† the content of Mo^{4+} species in $MoNi_4/MoO_x$ was higher than that in $MoNi_4/MoO_x$-30s and $MoNi_4/MoO_x$-90s, wherein the chemical state and relevant content of Ni and O species were almost identical (Fig. S14b and c†). Expectedly, $MoNi_4/MoO_x$-30s and $MoNi_4/MoO_x$-90s showed lower activity than $MoNi_4/MoO_x$, as shown in Fig. S15,† indicating that the improvement from Mo^{4+} might be a positive way to optimize the HER energetics.

Moreover, Tafel plots calculated from the LSV curves showed a small value of 29.9 mV dec^{-1} for $MoNi_4/MoO_x$, which was

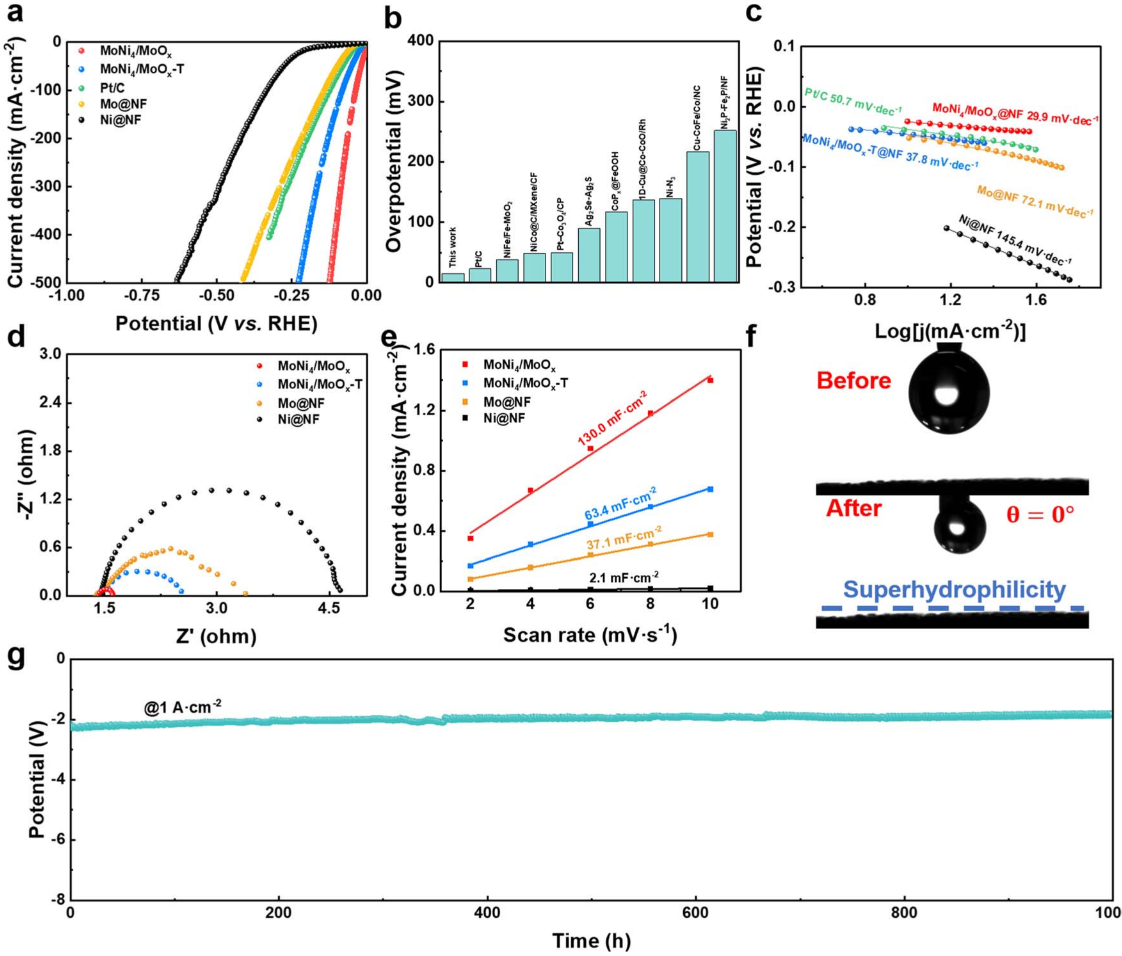

Fig. 4 (a) LSV curves of MoNi$_4$/MoO$_x$, MoNi$_4$/MoO$_x$-T, Pt/C, Mo@NF, and Ni@NF. (b) MoNi$_4$/MoO$_x$ HER performance compared with other electrocatalysts tested in alkaline seawater. Corresponding (c) Tafel plots of MoNi$_4$/MoO$_x$, MoNi$_4$/MoO$_x$-T, Pt/C, Mo@NF, and Ni@NF. Corresponding (d) EIS plots and (e) C_{dl} of MoNi$_4$/MoO$_x$, MoNi$_4$/MoO$_x$-T, Mo@NF, and Ni@NF. (f) Contact angle of MoNi$_4$/MoO$_x$. (g) Chronopotentiometry at 1 A cm^{-2} of MoNi$_4$/MoO$_x$ in alkaline seawater electrolyte.

lower than those of MoNi$_4$/MoO$_x$-T (37.8 mV dec^{-1}), Pt/C (50.7 mV dec^{-1}), Mo@NF (72.1 mV dec^{-1}), and Ni@NF (145.4 mV dec^{-1}) (Fig. 4c). The value of the Tafel plots indicated a faster reaction kinetics and implied a two-electron transfer process on the MoNi$_4$/MoO$_x$, which should follow a conventional Volmer–Tafel mechanism, with the rate-determining step (RDS) associated with the H_2 desorption (Tafel step).[51,52]

Furthermore, EIS measurements were employed to investigate the interfacial charge-transfer kinetics (Fig. 4d). Based on the Nyquist plots, which were analyzed with the respective fitted circuit diagram (Fig. S16†), MoNi$_4$/MoO$_x$ showed a minimum charge-transfer resistance (R_{ct}) of 0.18 Ω among all the samples, but 1.17 Ω for MoNi$_4$/MoO$_x$-T, indicating its much faster electron transport during the HER. This promoted electron transfer was not only due to the metallic MoNi$_4$ alloy but also a result of the abundant oxygen vacancies generated from the low valence states of Mo^{4+} and Mo^{5+}.[53]

Besides the interfacial charge-transfer ability, the number of exposed active sites plays an important role in achieving excellent HER activity. To get insights into the distinct merit of MoNi$_4$/MoO$_x$, the electrochemically active surface area (ECSA) was assessed, which reflects the HER performance of the as-prepared catalysts *via* the CV curves in the non-faradaic region. Typically, a series of CV measurements were performed for MoNi$_4$/MoO$_x$, MoNi$_4$/MoO$_x$-T, Mo@NF, and Ni@NF carried out under scan rates from 2 to 10 mV s^{-1} (Fig. S17a–d†). As shown in Fig. 4e, MoNi$_4$/MoO$_x$ possessed the highest value of C_{dl} (130.0 mF cm^{-2}) among MoNi$_4$/MoO$_x$-T (63.4 mF cm^{-2}), Mo@NF (37.1 mF cm^{-2}), and Ni@NF (2.1 mF cm^{-2}), which was positively correlated to the ESCA. Compared with MoNi$_4$/MoO$_x$-T, such a high value of electrochemical capacitance for MoNi$_4$/MoO$_x$ could be ascribed to the rough surface and good dispersibility formed by the rapid Joule heating,[24] which agreed with the results from the SEM and TEM analyses. In addition, the ESCA-normalized specific activity of MoNi$_4$/MoO$_x$ was analyzed, wherein MoNi$_4$/MoO$_x$ showed superior intrinsic HER performance than other reported state-of-the-art electrocatalysts, as shown in Fig. S18a, b and Table S1.† Moreover, the intrinsic catalytic activities of the as-prepared samples were detected based on the TOF. The number of active sites of the as-prepared samples was measured by the CVs in Fig. S19a–d† and the results are summarized in Table S2.† Furthermore, as shown in Fig. S19e,† $MoNi_4/MoO_x$ showed the highest value of TOF (34.86 s^{-1}) than $MoNi_4/MoO_x$-T (7.64 s^{-1}), Mo@NF (4.70 s^{-1}), and Ni@NF (20.88 s^{-1}) at 100 mV, indicating its enhanced intrinsic catalytic activity.

Apart from the catalytic activity, the electrochemical durability, as a crucial parameter for HER electrocatalysts, of $MoNi_4/MoO_x$ was also tested at a constant current density of 1 A cm^{-2} for 1000 h (Fig. 4g). During the long-term testing, $MoNi_4/MoO_x$ showed superb durability without noticeable activity degradation for the activity due to the *in situ*-formed hierarchical tandem-type structure.[32] The XRD pattern of $MoNi_4/MoO_x$ post electrolysis after 1 h (Fig. S20†) was obtained, and showed no visible change after the test at 1 A cm^{-2}, indicating the excellent catalytic durability and chemical composition. Such excellent long-time durability suggested its feasibility for practical application, especially in seawater, wherein chloride corrosion is considered a major challenge. Meanwhile, due to the presence of chloride ions in seawater, the chlorine evolution reaction (CER) might be generated, which would be converted to hypochlorite species in alkaline electrolyte and would compete with the oxygen evolution reaction (OER).[54] Here, the CER resistance performance of $MoNi_4/MoO_x$ was determined by a spectrophotometric method using *N*,*N*-diethyl-1,4-phenylenediamine. The content of hypochlorite species was determined by measuring the absorbance of the treated electrolysis solution, which was collected after 1000 h test at 1 A cm^{-2}. By comparing the measured absorbance with the standard curve (Fig. S21†), it was found that the content of hypochlorite remained basically the same before and after electrolysis (Table S3†), indicating the outstanding selectivity for seawater electrolysis. For comparison, we measured the electrolyte treated by using NF as the cathode for only 1 h (1 A cm^{-2}), wherein the generated hypochlorite was much higher concentration than $MoNi_4/MoO_x$. Such a result might due to the ultralow overpotential (<0.480 V) provided by the three-electrode system that included $MoNi_4/MoO_x$, wherein the overpotential window was 0–0.480 V to promote the OER in alkaline seawater.[54]

In addition to that, the hydrophilicity as decided by the chemical components and structure of the catalyst was measured, wherein the good wettability suggested an enhanced transfer of electrolytes and hydrogen bubbles due to the low interfacial adhesion energy.[55] As shown in Fig. 4f, the water was instantly absorbed by the solid surface, which was attributed to the 3D rugged morphology.

DFT calculations

To further interpret the increased electrolytic performance provided by the high ratio of Mo^{4+}/Mo^{5+} in $MoNi_4/MoO_x$, theoretical investigations were carried out based on DFT. First, the models of the MoO_2 and Mo_2O_5 crystals were chosen, which both crystallize in the orthorhombic *Cmcm* space group, and where the O^{2-} was bonded with equivalent Mo^{4+} and Mo^{5+} atoms, respectively. For confirmation of the valence difference between the two types of crystals, qualitative valence analysis was performed by Bader charge analysis, as shown in Fig. 5a and b. Moreover, the DOS (density of states) for the MoO_2 and Mo_2O_5 crystals were calculated (Fig. 5c), wherein the value at the Fermi level of the crystal containing Mo^{4+} was significantly improved compared to in Mo_2O_5, indicating the presence of

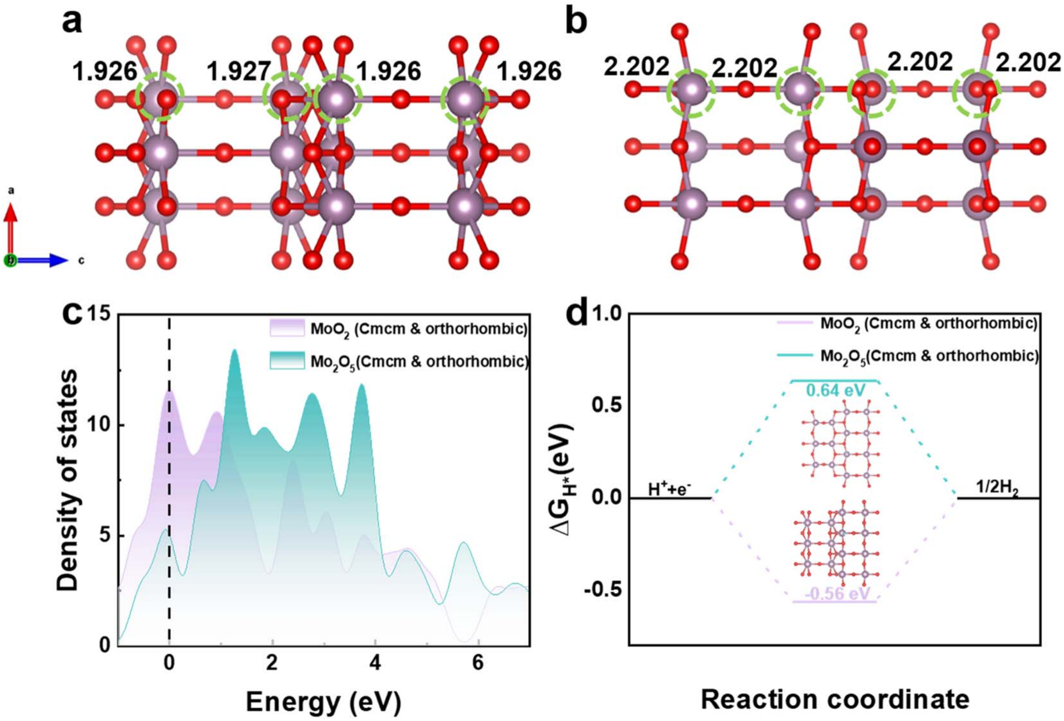

Fig. 5 (a and b) Bader charge analysis of Mo cations on MoO_2 and Mo_2O_5 crystals. (c) Calculated partial density of states (DOS) curves of MoO_2 and Mo_2O_5 crystals. (d) Calculated ΔG_{H*} values for H* adsorption on Mo sites of MoO_2 (010) and Mo_2O_5 (010).

more charge carriers and higher electrical conductivity.[56] Furthermore, guided by the Volmer–Heyrovsky mechanism, the hydrogen adsorption ability ΔG_{H^*} on the Mo sites were calculated, wherein a moderate ΔG_{H^*} that was close to zero is generally considered as the standard for excellent electrocatalysts.[57] The optimized structures of MoO_2 and Mo_2O_5 used for the calculation for the ΔG_{H^*} are shown in Fig. 5d. Fig. 5d shows that the H* adsorption energy on the top side of Mo^{4+} (−0.56 eV) was better than on Mo^{5+} (0.64 eV), leading to good proton adsorption and H desorption behaviors. Overall, the DFT results revealed the positive influence of Mo^{4+} on the HER performance, which accorded well with the electrochemical measurements.

Overall measurements of the water splitting activities

Considering the excellent performance for the HER, the overall water splitting (OWS) activities were also tested without *iR* compensation in alkaline seawater electrolyte, wherein the self-assembled $MoNi_4/MoO_x$ served as the cathode while the commercial RuO_2 served as the anode. As shown in Fig. 6a, the required potential for reaching 50 mA cm^{-2} was only 1.67 V for $MoNi_4/MoO_x//RuO_2$, which was much lower than that of the benchmark $Pt/C//RuO_2$ (1.93 V). Such a large gap indicated that $MoNi_4/MoO_x$ had the potential to serve as an active and cost-effective electrocatalyst for alkaline seawater splitting. Furthermore, the faradaic efficiency of $MoNi_4/MoO_x$ at 10 mA cm^{-2} in alkaline seawater was measured by the conventional drainage method (Fig. S22†). As shown in Fig. 6b, the H_2/O_2 volume ratio was close to 2 : 1, matching well to the calculated gaseous product evolution, which led to a ∼100% faradaic efficiency and indicating the high HER selectivity on the $MoNi_4/MoO_x$ cathode.

Measurements in a single stack of a commercial hydrogen generator

Besides, in order to confirm the feasibility of the application, we also combined $MoNi_4/MoO_x$ and Ni foam in a membrane electrode assembly (MEA) electrochemical reactor (Fig. 7a), with the commercial Ni foam//Ni foam also applied for comparison. In such a system, $MoNi_4/MoO_x$ was used as the cathode and Ni foam as the anode, separated by an alkaline exchange membrane as shown in Fig. 7b. As shown in Fig. 7c, the required voltage of 1.7 V was reached for the $MoNi_4/MoO_x$//Ni foam to drive 10 mA cm^{-2}, which was less than that required by Ni foam//Ni foam pairs of 2.1 V. Besides, with the introduction of $MoNi_4/MoO_x$, the needed voltages decreased to 2.01, 2.21, 2.37, and 2.51 V to achieve high current densities of 50, 100, 150, and 200 mA cm^{-2}, wherein the high voltage might due to the inherently poor conductivity of the add-on devices. Under a series of voltages, the relevant energy consumption was calculated to further reflect the superiority of our system in commercial applications. Table S4† presents the energy consumption under the different voltages, wherein the introduction of $MoNi_4/MoO_x$ was confirmed to visually improve the energy efficiency. Notably, the saved energy was up to 3.33 kW h m^{-3} at a voltage of 2.51 V (related to 200 mA cm^{-2}), as calculated by eqn (S1) in the ESI.† Remarkably, the $MoNi_4/MoO_x$//Ni foam displayed almost the same LSV curves under different flow rates, while the performance of the Ni foam//Ni foam system decreased under a lower flow rate (Fig. S23†), which might have been caused by the influence of hydrophilicity. Moreover, the durability of the MEA electrochemical reactor containing $MoNi_4/MoO_x$ was tested (Fig. 7d), and a performance improvement was observed during the initial period, which might have been caused by the adsorption of $Mo_2O_7{}^{2-}$ in alkaline seawater, which was formed by the leaching of Mo, as reported by Zhang *et al.*[58] Such a system exhibited good stability over 16 h at a constant 250 mA cm^{-2}, wherein a minor shift was noted caused by the influence of restarting the peristaltic pumps and indicating the feasibility of the system in practical applications.

Measurement in five stacks of commercial hydrogen generators

To highlight the significance for industrial applications, we further expanded the scale of the MEA electrochemical reactor

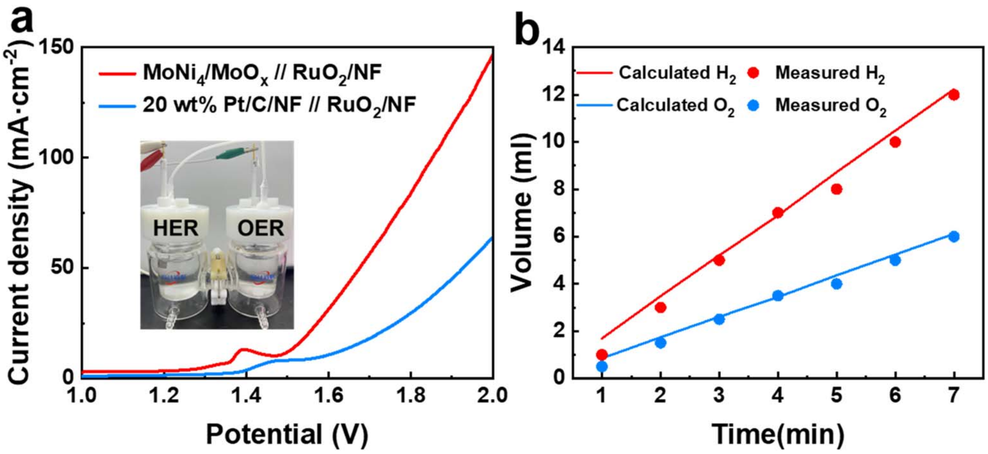

Fig. 6 (a) LSV curves without *iR* compensation in 1 M alkaline seawater electrolyte (the electrolyzer is shown in the inset image). (b) Amounts of the theoretical and evolved gases (H_2 and O_2) in alkaline seawater with a constant current density of 10 mA cm^{-2}.

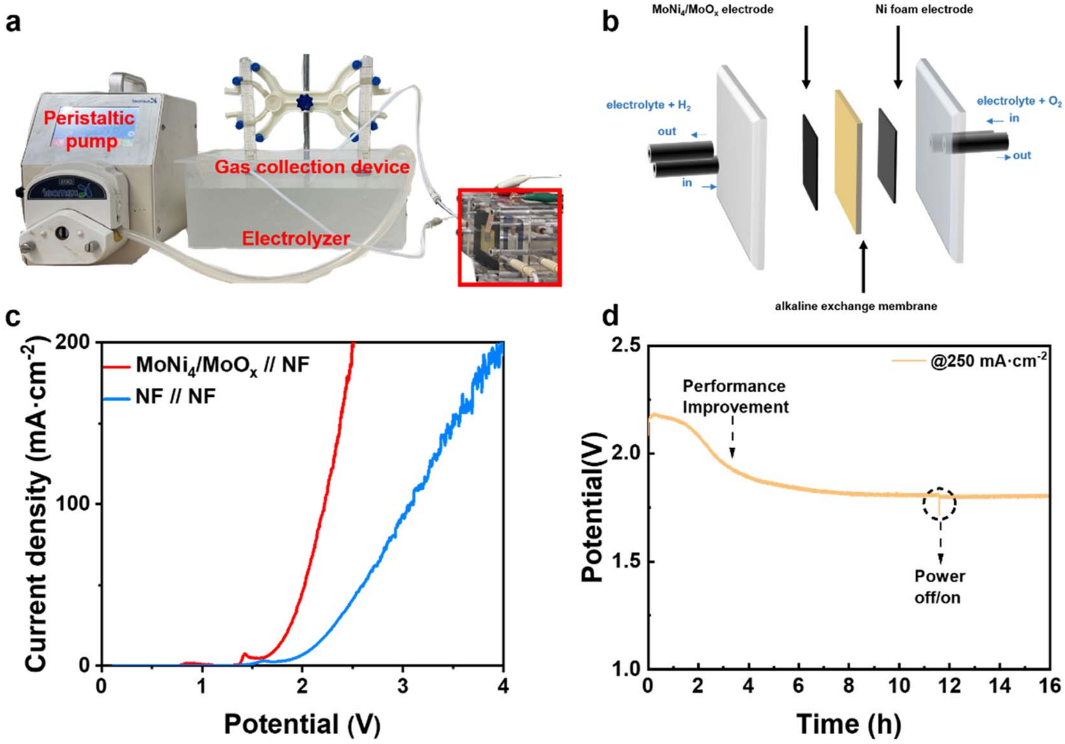

Fig. 7 (a) Photo of the hydrogen generator. (b) Schematic illustration of the MEA electrolyzer. (c) LSV curves in the MEA electrolyzer in 1 M alkaline seawater electrolyte without *iR* compensation. (d) Chronopotentiometric curves at 250 mA cm^{-2}.

by integrating five groups of $MoNi_4/MoO_x$ cathodes and Ni foam anodes with a DC motor (Fig. 8a and S24a–d†). The water electrolysis device could be connected in paralleled by wires to obtain the same voltage. Typically, the current density under different voltages with the $MoNi_4/MoO_x$//Ni foam were higher than with the commercial Ni foam//Ni foam (Fig. 8b), wherein the needed cell voltages, in the alkaline seawater at room temperature (20 °C), to achieve 100, 300, and 500 mA cm^{-2} were as low as 2.62, 3.75, and 4.66 V, respectively. Typically, the performance of the systems in the 50 °C electrolyte was improved to 2.32, 3.31, and 4.21 V to achieve 100, 300, and 500 mA cm^{-2}, noting the adaptability of $MoNi_4/MoO_x$ to perform in harsh operating conditions, which is noticeably favorable for its potential industrial application. Most importantly, the introduction of $MoNi_4/MoO_x$ was beneficial to the energy efficiency, with the calculated values listed in the ESI Table S5,† indicting its potential for scaling up production capabilities.

Measurements in a solar power-assisted water splitting device

Moreover, we fabricated a solar power-assisted water splitting device to reflect the superiority of $MoNi_4/MoO_x$ for sustainable application under AM 1.5G simulated solar power. A $MoNi_4/MoO_x$//RuO_2 electrolyzer was assembled in a series of PSCs for carbon-free hydrogen generation in alkaline seawater, wherein

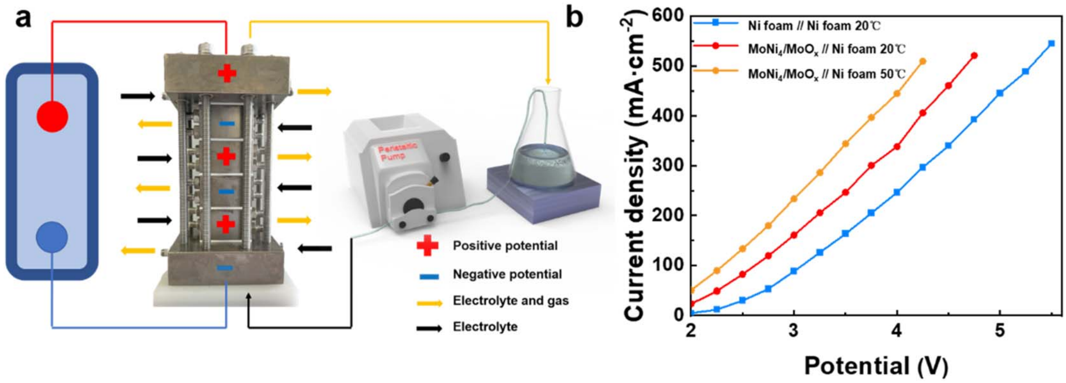

Fig. 8 (a) Schematic illustration of the scaled-up hydrogen generator system. (b) LSV curves in 1 M alkaline seawater electrolyte without *iR* compensation.

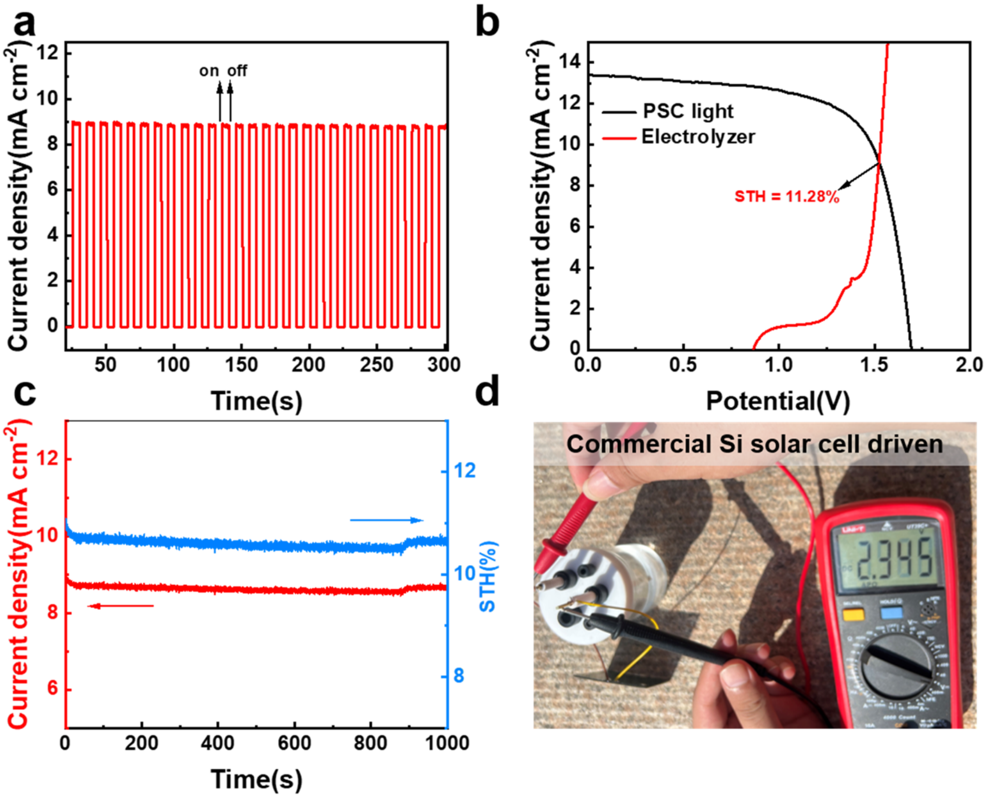

Fig. 9 (a) Transient photocurrent responses of the solar-driven system under chopped illumination. (b) Current density–potential curve of the alkaline seawater electrolyzer and tandem solar cells under simulated AM 1.5G 100 mW cm^{-2} illumination. (c) Stability test of the solar power-assisted water splitting device and corresponding STH efficiency. (d) Photo showing the alkaline seawater electrolyzer driven by a commercial silicon solar cell under a voltage of 2.345 V.

a tandem PSC was obtained by integrating two single PSCs to achieve enough photovoltage to drive seawater electrolysis. First, in order to confirm the light-driven reliability of such a system, transient photocurrent response measurements were performed under chopped illumination, wherein a constant operating current value could be rapidly obtained under illumination (Fig. 9a). Then, as shown in Fig. 9b, the *I*–*V* curves of the 2 PSCs in series module exhibited an open circuit voltage of 1.69 V and short circuit current density of 13.40 mA cm^{-2}. Typically, the theoretical operation current density of the solar power-assisted water splitting device was defined by the intersection point of the *I*–*V* curves (Fig. 9b) of the $MoNi_4/MoO_x$//RuO_2 system and PSC, which gave a value of 9.14 mA cm^{-2}, corresponding to a significantly high STH of 11.28%. In comparison, the theoretical operation current density of the Pt/C//RuO_2 system coupled with PSC was also calculated, which only exhibited an STH of 8.61%, as shown in Fig. S25.† Moreover, the actual current density and STH efficiency of such a system could be steadily maintained for 1000 s without noticeable fluctuation (Fig. 9c), illuminating the possibility for the combination of clean energy conversion and practical applications. Finally, the alkaline seawater electrolyzer coupled with a commercial silicon solar cell was integrated for performing outdoor solar tests (Fig. 9d), whereby the water splitting reaction could occur normally with an STH conversion efficiency of 7.3% (Fig. S26†).

Conclusion

In summary, we reported an ultrafast and facile strategy to synthesize a self-supported $MoNi_4/MoO_x$ cathode for highly active (15 mV @ 10 mA cm^{-2}, 227 mV @ 1000 mA cm^{-2}) and stable (1 A cm^{-2} @ 1000 h) seawater electrolysis by a simple process of Joule heating the $NiMoO_4$ precursor for only 60 s. Besides the advantages of only 0.12% energy consumption of the traditional heating process and ultrashort synthesis cycle, the $MoNi_4/MoO_x$ system exhibited better electrochemical properties than $MoNi_4/MoO_x$-T, which was not only due to the advantages of its structure but also the high content of Mo^{4+}, as revealed by DFT calculations. The combination of $MoNi_4/MoO_x$ and Ni foam in a membrane electrode assembly (MEA) electrochemical reactor was completed to give an OWS system, wherein the saved energy was up to 3.33 kW h m^{-3} at a current density of 200 mA cm^{-2} compared with the commercial Ni foam//Ni foam system. Finally, tests of the carbon-free hydrogen generation system upon AM 1.5G simulated solar power were carried out to realize 11.28% STH efficiency with long-stability, which illuminated the possibility for solar-driven hydrogen production in the future.

Experimental section

Synthesis of $NiMoO_4$

The NF was cut into 1 cm × 3 cm strips, and washed with 2 M HCl in an ultrasonic bath for 10 min in order to remove the oxide layer. Then, the NF was further ultrasonically cleaned to remove the organic species in acetone solution for 10 min. Finally, the as-treated NF was further washed with de-ionized (DI) water and ethanol three times.

The cleaned NF was transferred into a 20 mL Teflon-lined stainless-steel autoclave containing 40 mM of $Ni(NO_3)_2 \cdot 6H_2O$ and 10 mM of $(NH_4)_6Mo_7O_{24} \cdot 4H_2O$, which was heated at 150 °C for 6 h. After naturally cooling down to room temperature, the yellow-green sample coated on NF was taken out, washed with DI water three times, and dried in air for 12 h. The as-prepared sample was labeled as $NiMoO_4$.

Synthesis of $MoNi_4/MoO_x$

The synthesized $NiMoO_4$ was sandwiched between two molybdenum boats mounted on conductive carbon plates with a gap. The Joule heating was achieved by applying constant current to such a system. The sample was heated for 60 s at 500 °C under an Ar–H_2 (10%) flow. For comparison, samples ($MoNi_4/MoO_x$-*t*) with different heating times ($t = 30$, 90 s) were obtained under the same conditions. The preparation of Ni@NF was the same as that for $MoNi_4/MoO_x$ except that the $(NH_4)_6Mo_7O_{24} \cdot 4H_2O$ was removed during the synthesis of the precursor. The preparation of Mo@NF was the same as that of $MoNi_4/MoO_x$ except that the $Ni(NO_3)_2 \cdot 6H_2O$ was removed during the synthesis of the precursor. For comparison, the $NiMoO_4$ precursor was heated in a tube furnace, which was maintained at 500 °C for 2 h under 150 mL min^{-1} Ar–H_2 (10%) flow. After calcination, the obtained sample was named as $MoNi_4/MoO_x$-T.

Materials characterization

The crystal structure was recorded by X-ray diffraction (XRD) (Rigaku Miniflex 600). The X-ray photoelectron spectroscopy (XPS) analysis was carried out on a Thermo Scientific K-Alpha system. The morphology and structure of the obtained samples were tested using transmission electron microscopy (TEM) (JEOL JEM 2100) and scanning electron microscopy (SEM) (Zeiss Gemini 300) systems coupled with an energy dispersive spectrometry (EDS) unit. The Brunauer–Emmett–Teller (BET) surface area and Barrett–Joyner–Halenda model were tested on a Micromeritics ASAP 2460 system. A Dataphysics OCA 20 contact angle system was applied to test the hydrophilicity of the electrodes.

Electrochemical measurements

All the electrochemical measurements of the pre-synthesized samples were tested on an electrochemical workstation (CHI660E) coupled with a standard three-electrode system in alkaline seawater (pH 14). The as-prepared samples, Hg/HgO electrode, and graphite rod (3 mm in diameter) were used as the working electrode, reference electrode, and counter electrode, respectively. For comparison, 20 wt% Pt/C and RuO_2 electrodes were prepared. A homogeneous ink was formed by weighing and dispersing 20 wt% Pt/C and RuO_2 into Nafion solution (Nafion : ethanol = 1 : 10). Then, the ink was loaded on the NF to form a cathode and anode (2 mg cm^{-2}). The measured potentials *versus* Hg/HgO reference electrode were transformed into RHE by the equation $E_{RHE} = E_{SCE} + 0.098\ V + 0.0592pH$, with removing the *IR* drop. To evaluate the electrocatalytic activity of the catalysts, linear sweep voltammetry (LSV) tests were performed at a scan rate of 5 mV s^{-1} and Tafel slopes could be obtained from the LSV curves. In order to investigate the double-layer capacitance values (C_{dl}), cyclic voltammetry (CV) curves were measured at different scan rates (from 2 to 10 mV s^{-1}). The electrochemical impedance spectroscopy (EIS) measurements were performed with the frequency range from 10^{-5} to 10^{-2} Hz. A two-electrode configuration was used to test the overall seawater splitting activity. The stability tests for the HER were conducted under a constant current density without *iR* drop compensation. The faradaic efficiency (FE) was calculated by the following equations: $FE = Q_E/Q_T$, $N_E = V_0/V_m$, $N_T = Q/(n \times F)$, where F is the faradaic constant (96 500 C mol^{-1}), Q_E is the number of hydrogens measured by the water drainage method, Q_T is the theoretical number of hydrogens, V_0 is the actual volume of hydrogen, V_m is 22.4 L mol^{-1}, Q is the number of charges transferred, and n is 2 (for HER). The H_2 turnover frequency (TOF) was calculated by the following equation: $TOF = j \times N_A/(F \times n \times m)$, where j is the current density obtained from the LSV; N_A is the Avogadro constant; F is the faradaic constant (96 500 C mol^{-1}); and n is the number of electrons transferred to generate one molecule of hydrogen (n is 2 for HER), with the number of active sites calculated by the CV test in alkaline seawater (pH 14), which ranged from 0 V to 0.6 V (*vs.* RHE) at a scan rate of 50 mV s^{-1}.

The tests in the membrane electrode assembly (MEA) electrochemical reactor used a Ti-5MEA-2020 coupled with an electrochemical workstation, wherein the anion-exchange membrane (FAA-3-50) prevented the interference of H_2 and O_2.

Density functional theory (DFT) calculations

First-principle calculations were carried out *via* the Vienna *ab initio* simulation package, wherein the gradient approximation with the Perdew–Burke–Ernzerhof (PBE) parameterization was confirmed as the electron exchange–correlation function. For the structure optimization, the energy convergence criterion was set to 10^{-5} eV and -001 eV $Å^{-1}$. The plane-wave cutoff energy was converged to 300 eV and a 3 × 3 × 1 *k*-point mesh was set for the geometry optimization. The adsorption energy for the adsorbed species were obtained by using the equation: $\Delta G = \Delta E + \Delta ZPE - T\Delta S$, wherein ΔE represents the chemisorption energy.

Fabrication of a solar-driven electrolysis system

The solar-driven electrolysis system was analyzed by KEITHLET 2400 and CHI660 systems, wherein a 300 W xenon lamp with an AM 1.5G optical filter (100 mW cm^{-2}) was used as the solar simulator. PSCs (0.068 cm^{-2}) were fabricated in a glovebox, which could maintain the temperature (20 °C), oxygen (0.1 ppm), and water (0.1 ppm) conditions. The additive was prepared by dissolving blends of D18, Y6, and BTP-eC9 active layers in chloroform with 0.5 vol% 1,8-diiodooctane (DIO). Indium tin oxide (ITO) glass was applied as the substrate, wherein the devices were fabricated with the structure of: ITO/PEDOT:PSS/active layer/PDINO/Al. UV-ozone treatment of the ITO was performed after its sonication treatment in detergent solution, acetone, and isopropanol sequentially. A PEDOT:PSS (CLEVIOS PVP AI 4083) thin film (40 nm) was spin-coated on top of the cleaned ITO substrate at 4000 rpm for 30 s, followed by thermal annealing at 150 °C for 15 min. Then, the active layer was deposited on top of the PEDOT:PSS layer at 3000 rpm for 35 s followed by annealing at 100 °C for 10 min. After that, a layer of PDINO in methanol was spin-coated onto the active layer at 3000 rpm for 30 s and Al with a thickness of 80 nm was deposited *via* thermal evaporation under 4×10^{-4} Pa. To achieve enough photovoltage to drive the seawater electrolysis, two single PSCs were integrated in series, which were connected with the $MoNi_4/MoO_x//RuO_2$ electrolyzer to form a solar-driven electrolysis system. The STH of such system was calculated by the formula: $\text{STH}\ (\%) = I\ (\text{mA cm}^{-2}) \times 1.23\ (\text{V}) \times 100/P_{\text{sun}}$, where I is the current density of the solar-driven electrolysis system and P_{sun} is the incident simulated solar energy. A commercial silicon solar cell was connected with the electrolyzer for the outdoors tests.

Conflicts of interest

There are no conflicts to declare.

Acknowledgements

The authors acknowledge the financial supports from National Natural Science Foundation of China (Grant No. 22002146), Taishan Scholars Foundation of Shandong Province (No. tsqn201909058, tsqn201812026), Shandong Provincial Natural Science Foundation (Grant No. ZR2021QB056), and Qingdao Zhongshida New Energy Technology Co. (Contract No. 20220114).

References

1 J. Wang, F. Xu, H. Jin, Y. Chen and Y. Wang, Non-noble metal-based carbon composites in hydrogen evolution reaction: fundamentals to applications, *Adv. Mater.*, 2017, **29**, 1605838–1605873.

2 X. Zheng, Y. Chen, X. Bao, S. Mao, R. Fan and Y. Wang, *In situ* formed bimetallic carbide Ni_6Mo_6C nanodots and $NiMoO_x$ nanosheet array hybrids anchored on carbon cloth: efficient and flexible self-supported catalysts for hydrogen evolution, *ACS Catal.*, 2020, **10**, 11634–11642.

3 Z. Zhou, Z. Pei, L. Wei, S. Zhao, X. Jian and Y. Chen, Electrocatalytic hydrogen evolution under neutral pH conditions: current understandings, recent advances, and future prospects, *Energy Environ. Sci.*, 2020, **13**, 3185–3206.

4 X. Zhang, S. Zhang, J. Li and E. Wang, One-step synthesis of well-structured $NiS–Ni_2P_2S_6$ nanosheets on nickel foam for efficient overall water splitting, *J. Mater. Chem. A*, 2017, **5**, 22131–22136.

5 J. Sun, Z. Zhang and X. Meng, Low-Pt supported on MOF-derived $Ni(OH)_2$ with highly-efficiently electrocatalytic seawater splitting at high current density, *Appl. Catal., B*, 2023, **331**, 122703–122713.

6 Z. Zhao, J. Sun and X. Meng, Recent advances in transition metal-based electrocatalysts for seawater electrolysis, *Int. J. Energy Res.*, 2022, **46**, 17952–17975.

7 J. Li, J. Sun, Z. Li and X. Meng, Recent advances in electrocatalysts for seawater splitting in hydrogen evolution reaction, *Int. J. Hydrogen Energy*, 2022, **47**, 29685–29697.

8 J. Sun, J. Li, Z. Li, X. Hu, H. Bai and X. Meng, Phase Transition in Cobalt Selenide with a Greatly Improved Electrocatalytic Activity in Hydrogen Evolution Reactions, *ACS Sustainable Chem. Eng.*, 2022, **10**, 4022–4030.

9 J. Sun, J. Li, Z. Li, C. Li, G. Ren, Z. Zhang and X. Meng, Modulating the Electronic Structure on Cobalt Sites by Compatible Heterojunction Fabrication for Greatly Improved Overall Water/Seawater Electrolysis, *ACS Sustainable Chem. Eng.*, 2022, **10**, 9980–9990.

10 M. K. Debe, Electrocatalyst approaches and challenges for automotive fuel cells, *Nature*, 2012, **486**, 43–51.

11 Y. Li, Q. Gu, B. Johannessen, Z. Zheng, C. Li, Y. Luo, Z. Zhang, Q. Zhang, H. Fan, W. Luo, B. Liu, S. Dou and H. Liu, Synergistic Pt doping and phase conversion engineering in two-dimensional MoS_2 for efficient hydrogen evolution, *Nano Energy*, 2021, **84**, 105898–105906.

12 C. Pi, C. Huang, Y. Yang, H. Song, X. Zhang, Y. Zheng, B. Gao, J. Fu, P. K. Chu and K. Huo, *In situ* formation of N-doped carbon-coated porous MoP nanowires: a highly efficient electrocatalyst for hydrogen evolution reaction in a wide pH range, *Appl. Catal., B*, 2020, **263**, 118358–118365.

13 H. Zeng, S. Chen, Y. Q. Jin, J. Li, J. Song, Z. Le, G. Liang, H. Zhang, F. Xie, J. Chen, Y. Jin, X. Chen and H. Meng, Electron density modulation of metallic MoO_2 by Ni doping to produce excellent hydrogen evolution and oxidation activities in acid, *ACS Energy Lett.*, 2020, **5**, 1908–1915.

14 H. Vrubel and X. Hu, Molybdenum boride and carbide catalyze hydrogen evolution in both acidic and basic solutions, *Angew. Chem., Int. Ed.*, 2012, **51**, 12703–12706.

15 L.-B. Huang, L. Zhao, Y. Zhang, Y.-Y. Chen, Q.-H. Zhang, H. Luo, X. Zhang, T. Tang, L. Gu and J.-S. Hu, Self-limited on-site conversion of MoO_3 nanodots into vertically aligned ultrasmall monolayer MoS_2 for efficient hydrogen evolution, *Adv. Energy Mater.*, 2018, **8**, 1800734–1800741.

16 Z. Wang, W. Liu, Y. Hu, M. Guan, L. Xu, H. Li, J. Bao and H. Li, Cr-doped CoFe layered double hydroxides: Highly efficient and robust bifunctional electrocatalyst for the oxidation of water and urea, *Appl. Catal., B*, 2020, **272**, 118959.

17 L. Yang, L. Zeng, H. Liu, Y. Deng, Z. Zhou, J. Yu, H. Liu and W. Zhou, Hierarchical microsphere of MoNi porous

nanosheets as electrocatalyst and cocatalyst for hydrogen evolution reaction, *Appl. Catal., B*, 2019, **249**, 98–105.

18 A. Nairan, P. Zou, C. Liang, J. Liu, D. Wu, P. Liu and C. Yang, NiMo solid solution nanowire array electrodes for highly efficient hydrogen evolution reaction, *Adv. Funct. Mater.*, 2019, **29**, 1903747–1903755.

19 M. Xia, T. Lei, N. Lv and N. Li, Synthesis and electrocatalytic hydrogen evolution performance of Ni–Mo–Cu alloy coating electrode, *Int. J. Hydrogen Energy*, 2014, **39**, 4794–4802.

20 J. Zhang, T. Wang, P. Liu, Z. Liao, S. Liu, X. Zhuang, M. Chen, E. Zschech and X. Feng, Efficient hydrogen production on $MoNi_4$ electrocatalysts with fast water dissociation kinetics, *Nat. Commun.*, 2017, **8**, 15437–15445.

21 L. Guo, Q. Yu, X. Zhai, J. Chi, T. Cui, Y. Zhang, J. Lai and L. Wang, Reduction-induced interface reconstruction to fabricate $MoNi_4$-based hollow nanorods for hydrazine oxidation assisted energy-saving hydrogen production in seawater, *Nano Res.*, 2022, **15**, 8846–8856.

22 J. Sun, Z. Zhao, J. Li, Z. Li and X. Meng, Recent advances in transition metal selenides-based electrocatalysts: Rational design and applications in water splitting, *J. Alloys Compd.*, 2022, **918**, 165719–165737.

23 H. Huang, S. Zhou, C. Yu, H. Huang, J. Zhao, L. Dai and J. Qiu, Rapid and energy-efficient microwave pyrolysis for high-yield production of highly-active bifunctional electrocatalysts for water splitting, *Energy Environ. Sci.*, 2020, **13**, 545–553.

24 F. Yang, Y. Luo, Q. Yu, Z. Zhang, S. Zhang, Z. Liu, W. Ren, H. M. Cheng, J. Li and B. Liu, A durable and efficient electrocatalyst for saline water splitting with current density exceeding 2000 mA cm^{-2}, *Adv. Funct. Mater.*, 2021, **31**, 2010367–2010377.

25 Y. Y. Chen, Y. Zhang, X. Zhang, T. Tang, H. Luo, S. Niu, Z. H. Dai, L. J. Wan and J. S. Hu, Self-templated fabrication of $MoNi_4/MoO_{3-x}$ nanorod arrays with dual active components for highly efficient hydrogen evolution, *Adv. Mater.*, 2017, **29**, 1703311–1703318.

26 Y. Sun, C. Liu, D. C. Grauer, J. Yano, J. R. Long, P. Yang and C. J. Chang, Electrodeposited cobalt-sulfide catalyst for electrochemical and photoelectrochemical hydrogen generation from water, *J. Am. Chem. Soc.*, 2013, **135**, 17699–17702.

27 Y. Chen, S. Xu, S. Zhu, R. J. Jacob, G. Pastel, Y. Wang, Y. Li, J. Dai, F. Chen, H. Xie, B. Liu, Y. Yao, L. G. Salamanca-Riba, M. R. Zachariah, T. Li and L. Hu, Millisecond synthesis of CoS nanoparticles for highly efficient overall water splitting, *Nano Res.*, 2019, **12**, 2259–2267.

28 Y. Chen, S. Xu, Y. Li, R. J. Jacob, Y. Kuang, B. Liu, Y. Wang, G. Pastel, L. G. Salamanca-Riba, M. R. Zachariah and L. Hu, FeS_2 nanoparticles embedded in reduced graphene oxide toward robust, high-performance electrocatalysts, *Adv. Energy Mater.*, 2017, **7**, 1700482–1700489.

29 L. Xing, R. Liu, Z. Gong, J. Liu, J. Liu, H. Gong, K. Huang and H. Fei, Ultrafast Joule heating synthesis of hierarchically porous graphene-based Co-N-C single-atom monoliths, *Nano Res.*, 2021, **15**, 3913–3919.

30 X. Liu, K. Ni, C. Niu, R. Guo, W. Xi, Z. Wang, J. Meng, J. Li, Y. Zhu, P. Wu, Q. Li, J. Luo, X. Wu and L. Mai, Upraising the O 2p Orbital by Integrating Ni with MoO_2 for Accelerating Hydrogen Evolution Kinetics, *ACS Catal.*, 2019, **9**, 2275–2285.

31 G. Xiong, Y. Chen, Z. Zhou, F. Liu, X. Liu, L. Yang, Q. Liu, Y. Sang, H. Liu, X. Zhang, J. Jia and W. Zhou, Rapid synthesis of various electrocatalysts on Ni foam using a universal and facile induction heating method for efficient water splitting, *Adv. Funct. Mater.*, 2021, **31**, 2009580–2009591.

32 B. Lin, J. Chen, R. Yang, S. Mao, M. Qin and Y. Wang, Multi-hierarchical cobalt-based electrocatalyst towards high rate H_2 production, *Appl. Catal., B*, 2022, **316**, 121666–121678.

33 L. Yu, Q. Zhu, S. Song, B. McElhenny, D. Wang, C. Wu, Z. Qin, J. Bao, Y. Yu, S. Chen and Z. Ren, Non-noble metal-nitride based electrocatalysts for high-performance alkaline seawater electrolysis, *Nat. Commun.*, 2019, **10**, 5106.

34 L. Wu, L. Yu, B. McElhenny, X. Xing, D. Luo, F. Zhang, J. Bao, S. Chen and Z. Ren, Rational design of core-shell-structured CoP@FeOOH for efficient seawater electrolysis, *Appl. Catal., B*, 2021, **294**, 120256–120265.

35 M. Thommes, K. Kaneko, A. V. Neimark, J. P. Olivier, F. Rodriguez-Reinoso, J. Rouquerol and K. S. W. Sing, Physisorption of gases, with special reference to the evaluation of surface area and pore size distribution (IUPAC Technical Report), *Pure Appl. Chem.*, 2015, **87**, 1051–1069.

36 S. Dou, J. Xu, X. Cui, W. Liu, Z. Zhang, Y. Deng, W. Hu and Y. Chen, High-temperature shock enabled nanomanufacturing for energy-related applications, *Adv. Energy Mater.*, 2020, **10**, 2001331–2001346.

37 S. Crouch-Baker and P. Dickens, Standard molar enthalpies of formation of $MoO_3 \cdot 2H_2O$ and yellow $MoO_3 \cdot H_2O$ by solution calorimetry, *J. Chem. Thermodyn.*, 1983, **15**, 675–679.

38 X. Wang, R. Su, H. Aslan, J. Kibsgaard, S. Wendt, L. Meng, M. Dong, Y. Huang and F. Besenbacher, Tweaking the composition of NiMoZn alloy electrocatalyst for enhanced hydrogen evolution reaction performance, *Nano Energy*, 2015, **12**, 9–18.

39 X. Yuan, H. Ge, X. Wang, C. Dong, W. Dong, M. S. Riaz, Z. Xu, J. Zhang and F. Huang, Controlled phase evolution from Co nanochains to CoO nanocubes and their application as OER catalysts, *ACS Energy Lett.*, 2017, **2**, 1208–1213.

40 G. Liu, H. Bai, Y. Ji, L. Wang, Y. Wen, H. Lin, L. Zheng, Y. Li, B. Zhang and H. Peng, A highly efficient alkaline HER Co–Mo bimetallic carbide catalyst with an optimized Mo d-orbital electronic state, *J. Mater. Chem. A*, 2019, **7**, 12434–12439.

41 C. Niu, X. Liu, J. Meng, L. Xu, M. Yan, X. Wang, G. Zhang, Z. Liu, X. Xu and L. Mai, Three dimensional V_2O_5/NaV_6O_{15} hierarchical heterostructures: Controlled synthesis and synergistic effect investigated by *in situ* X-ray diffraction, *Nano Energy*, 2016, **27**, 147–156.

42 W. Shi, J. Zhu, L. Gong, D. Feng, Q. Ma, J. Yu, H. Tang, Y. Zhao and S. Mu, Fe-incorporated Ni/MoO_2 hollow

heterostructure nanorod arrays for high-efficiency overall water splitting in alkaline and seawater media, *Small*, 2022, 2205683–2205692.

43 F. Sun, J. Qin, Z. Wang, M. Yu, X. Wu, X. Sun and J. Qiu, Energy-saving hydrogen production by chlorine-free hybrid seawater splitting coupling hydrazine degradation, *Nat. Commun.*, 2021, **12**, 4182–4193.

44 K. Xiang, Z. Song, D. Wu, X. Deng, X. Wang, W. You, Z. Peng, L. Wang, J.-L. Luo and X.-Z. Fu, Bifunctional Pt–Co_3O_4 electrocatalysts for simultaneous generation of hydrogen and formate *via* energy-saving alkaline seawater/methanol co-electrolysis, *J. Mater. Chem. A*, 2021, **9**, 6316–6324.

45 L. Yang, C. Feng, C. Guan, L. Zhu and D. Xia, Construction of seaurchin-like structured Ag_2Se-Ag_2S-CoCH/NF electrocatalyst with high catalytic activity and corrosion resistance for seawater electrolysis, *Appl. Surf. Sci.*, 2023, **607**, 154885–154900.

46 W. Zang, T. Sun, T. Yang, S. Xi, M. Waqar, Z. Kou, Z. Lyu, Y. P. Feng, J. Wang and S. J. Pennycook, Efficient hydrogen evolution of oxidized Ni-N_3 defective sites for alkaline freshwater and seawater electrolysis, *Adv. Mater.*, 2021, **33**, 2003846–2003854.

47 L. Wu, L. Yu, B. McElhenny, X. Xing, D. Luo, F. Zhang, J. Bao, S. Chen and Z. Ren, Rational design of core-shell-structured CoP@FeOOH for efficient seawater electrolysis, *Appl. Catal., B*, 2021, **294**, 120256–120265.

48 P. K. L. Tran, D. T. Tran, D. Malhotra, S. Prabhakaran, D. H. Kim, N. H. Kim and J. H. Lee, Highly effective freshwater and seawater electrolysis enabled by atomic Rh-modulated Co-CoO lateral heterostructures, *Small*, 2021, **17**, 2103826–2103839.

49 X. Liu, H. Mao, G. Liu, Q. Yu, S. Wu, B. Li, G. Zhou, Z. Li and L. Wang, Metal doping and hetero-engineering of Cu-doped CoFe/Co embedded in N-doped carbon for improving trifunctional electrocatalytic activity in alkaline seawater, *Chem. Eng. J.*, 2023, **451**, 138699–138707.

50 L. Wu, L. Yu, F. Zhang, B. McElhenny, D. Luo, A. Karim, S. Chen and Z. Ren, Heterogeneous bimetallic phosphide Ni_2P-Fe_2P as an efficient bifunctional catalyst for water/seawater splitting, *Adv. Funct. Mater.*, 2021, **31**, 2006484–2006496.

51 J. X. Feng, J. Q. Wu, Y. X. Tong and G. R. Li, Efficient Hydrogen Evolution on Cu Nanodots-Decorated Ni_3S_2 Nanotubes by Optimizing Atomic Hydrogen Adsorption and Desorption, *J. Am. Chem. Soc.*, 2018, **140**, 610–617.

52 K. L. Zhou, Z. Wang, C. B. Han, X. Ke, C. Wang, Y. Jin, Q. Zhang, J. Liu, H. Wang and H. Yan, Platinum single-atom catalyst coupled with transition metal/metal oxide heterostructure for accelerating alkaline hydrogen evolution reaction, *Nat. Commun.*, 2021, **12**, 3783.

53 H. S. Kim, J. B. Cook, H. Lin, J. S. Ko, S. H. Tolbert, V. Ozolins and B. Dunn, Oxygen vacancies enhance pseudocapacitive charge storage properties of MoO_{3-x}, *Nat. Mater.*, 2017, **16**, 454–460.

54 S. Khatun, H. Hirani and P. Roy, Seawater electrocatalysis: activity and selectivity, *J. Mater. Chem. A*, 2021, **9**, 74–86.

55 K. Dastafkan, Q. Meyer, X. Chen and C. Zhao, Efficient oxygen evolution and gas bubble release achieved by a low gas bubble adhesive iron-nickel vanadate electrocatalyst, *Small*, 2020, **16**, 2002412–2022424.

56 Y. Cheng, H. Guo, P. Yuan, X. Li, L. Zheng and R. Song, Self-supported bifunctional electrocatalysts with Ni nanoparticles encapsulated in vertical N-doped carbon nanotube for efficient overall water splitting, *Chem. Eng. J.*, 2021, **413**, 127531–127539.

57 P. Li, X. Duan, S. Wang, L. Zheng, Y. Li, H. Duan, Y. Kuang and X. Sun, Amorphous ruthenium-sulfide with isolated catalytic sites for Pt-like electrocatalytic hydrogen production over whole pH range, *Small*, 2019, **15**, 1904043–1904051.

58 W. Du, Y. Shi, W. Zhou, Y. Yu and B. Zhang, Unveiling the *in situ* dissolution and polymerization of Mo in Ni_4Mo alloy for promoting the hydrogen evolution reaction, *Angew. Chem., Int. Ed.*, 2021, **60**, 7051–7055.